PAPER

Check for updates

Controlled synthesis of Sn-based oxides *via* a hydrothermal method and their visible light photocatalytic performances†

Jinghui Wang,[a] Hui Li,[a] Sugang Meng, [ID][a] Xiangju Ye,*[b] Xianliang Fu [ID]*[a] and Shifu Chen[ab]

Controlled synthesis of Sn-based oxides with a different valence state is still a challenge. Here, we developed a facile hydrothermal method for selective preparation of SnO_2, Sn^{2+} doped SnO_2 (Sn^{2+}−SnO_2), and SnO/SnO_2 composites, and SnO with $SnCl_2$ as a precursor. The valence state of Sn was regulated successively from Sn^{4+} to Sn^{2+} through controlling the hydrothermal solution from an O_2-rich to an O_2-deficient atmosphere, which was achieved by adding H_2O_2 or urea into the solution. The structure, absorption, morphology, and the visible light photocatalytic performance of the products were investigated systematically. SnO_2, Sn^{2+}−SnO_2, SnO/SnO_2, and SnO could be prepared in a H_2O_2-contained, H_2O, urea-contained, and N_2 purged urea-contained solution, respectively. For Sn^{2+}−SnO_2, the doping amount of Sn^{2+} could be further tuned by varying the hydrothermal temperature, while for SnO/SnO_2, the coupling amount of SnO could be controlled by the dosage of urea. Visible-light-induced photocatalytic degradation of methyl orange was achieved successfully on Sn^{2+}−SnO_2 and SnO/SnO_2. However, further work is still required to improve the stability of the samples due to vulnerability of Sn^{2+}.

1. Introduction

As a variable valence metal, Sn-based oxides can be in the form of univalent (SnO and SnO_2) or heterovalent oxides (Sn_2O_3 and Sn_3O_4, formed by regulating Sn^{2+}/Sn^{4+} ratio[1]). The univalent SnO and SnO_2 have attracted considerable attention during the past years because of their excellent optical, electrical, and electrochemical properties.[2–8] For SnO, it can be used as anode materials in Li-batteries,[7] coating materials,[9] and catalysts for cyclization of maleamic acid.[9] Furthermore, as Sn^{2+} can be easily oxidized to Sn^{4+} through a heat treatment in air, it can be used as a sacrificial template to prepare SnO_2, another versatile Sn oxide. Due to its high optical transparency in the visible range, the remarkable receptivity to variation of gas, the low resistivity, and the excellent chemical stability, SnO_2 has been extensively used in transparent conductive electrodes,[4] gas sensors,[10,11] Li-batteries,[5] sensitized solar cells,[12] and photocatalysts.[13–15] To optimize the SnO and SnO_2 performances,

various preparation methods including sol–gel, precipitation, hydrothermal, solvothermal, thermal evaporation, electro-spinning, and laser ablation have been developed to manipulate their sizes, structures, and morphologes.[8] Taking SnO_2 as an example, the particle size can be reduced through a surfactant-assisted solvothermal[16] or hydrothermal[17,18] route, while as for the morphologies, 0 to 3 dimensional SnO_2 nanostructures, such as nanoparticles, nanorods, nanowires, nanotube, nanosheets, and the 3D hierarchical architectures self-assembled from these low-dimensional nanostructures, have been subtly fabricated.[8] Although the structure and the morphology of the Sn oxides can be readily controlled by using different preparation routes, there still is a lacks of a versatile fabrication route to control the component of the product, which is a key prerequisite for the applications. Most of the preparation methods are only suitable for the preparation of one of the Sn oxides.

Semiconductor-based photocatalytic technology possesses a great potential in the environmental remediation for its "green", high efficiency, and broad applicability.[19,20] Photocatalytic degradation of pollutants on Sn oxides, especially SnO_2, has been extensively investigated. Unfortunately, as a well-known n-type semiconductor, SnO_2 can only be activated under UV irradiation due to the wide-band gap energy (3.5–3.8 eV).[21–23] Furthermore, the activity is significantly restricted by the quick recombination of photo-induced charge carriers ($e^−$ and h^+). Although the separation of $e^−$ and h^+ can be improved by compositing SnO_2 with TiO_2,[24,25] ZnO[26,27] and Zn_2SnO_4,[28,29] extending SnO_2 absorption to visible light range which accounts

[a]*College of Chemistry and Material Science, Huaibei Normal University, Huaibei, Anhui, 235000, China. E-mail: fuxiliang@gmail.com; Fax: +86-561-3090518; Tel: +86-561-3802235*

[b]*Department of Chemistry, Anhui Science and Technology University, Fengyang, Anhui, 233100, China. E-mail: yexiangju555@126.com*

† Electronic supplementary information (ESI) available: Degradation reaction system for MO, XPS spectrum of the prepared samples, time dependent UV-vis absorption spectrum of MO solution, chemical structure of MO, schematic band structures of the prepared samples, time dependent fluorescence spectra of the formed TAOH. See DOI: 10.1039/c7ra04041e

for 43% of the solar spectrum is still required to maximize the utilization of sunlight. Doping (non)-metallic elements is an effective strategy to narrow the band gap. However, the sample thermal stability and the separation of e^- and h^+ are generally hampered by the doping with heterogeneous elements. These disadvantages can be avoided by a self-doping approach,[30–33] which introduces no impurity elements into the sample. The validity of the self-doping has been confirmed on the Ti^{3+} doped TiO_2 and some Sn^{2+} doped Sn ternary oxides (Sn^{2+}–SnM_2O_6, M = Ta or Nb).[34–36]

Meanwhile, some other reports noted that SnO incorporated samples have a significant visible light activity in the degradation of organic pollutants.[1,37–40] These works arouse our interest that the visible light photocatalytic performance of SnO_2 may also can be promoted by doping with Sn^{2+} or incorporating with some Sn^{2+}-contained species like SnO, Sn_2O_3 or Sn_3O_4. The visible light photocatalytic performances of some Sn^{2+}-contained samples, such as SnO_{2-x},[41] Sn_3O_4,[42] SnO–TiO_2,[43] SnO/Sn_3O_4,[1] and Sn_3O_4/TiO_2,[44] demonstrate the feasibility of the strategy.

However, it remains difficult to incorporate Sn^{2+} species into SnO_2 as Sn^{2+} is easily oxidized to Sn^{4+}. Controlling the Sn oxidation state is still a critical challenge. Recently, Fan's work[41] indicates that Sn^{2+} self-doped SnO_2 can be skilfully prepared by a synproportionation reaction by adding Sn powder to the reaction solution: $Sn + Sn^{4+} \rightarrow Sn^{2+}$, while another work indicated that SnO and SnO_2 can be selectively prepared by controlling the solution pH.[45] These methods are limited to the preparation of one or two kinds of the Sn oxides. As far as we know, a facile method to synthesize a series of Sn oxides in a controlled way is still highly desired.

Herein, we developed a simple hydrothermal method to selective prepare a series of Sn oxides. Including SnO_2, Sn^{2+} doped SnO_2 (Sn^{2+}–SnO_2), SnO/SnO_2 composite, and SnO were successfully synthesized through controlling the solution composition. The visible light photocatalytic performance of the samples was then evaluated by the degradation of methyl orange (MO) solution.

2. Experiments

2.1 Chemicals and preparation of Sn oxides

Analytical grade $SnCl_2 \cdot 2H_2O$, urea ($CO(NH_2)_2$), H_2O_2, and MO were purchased from Aladdin Reagent Co. Ltd, Shanghai, China and used as received.

Preparation of Sn^{2+}–SnO_2. 1 g $SnCl_2 \cdot 2H_2O$ was dissolved in 80 mL deionized water. After stirring for 30 min, the solution was then transferred into a Teflon-lined stainless autoclave and maintained at an elevated temperature for 24 h. The yellow products were centrifuged and rinsed alternatively in water and ethanol, and finally dried at 60 °C in a vacuum oven.

Preparation of SnO/SnO_2. SnO/SnO_2 was prepared via a similar hydrothermal process in urea-contained solution at 160 °C for 24 h.

Preparation of SnO and SnO_2. Pristine SnO_2 and SnO were synthesized in H_2O with 3 g urea added. For the preparation of SnO_2, 1 mL H_2O_2 (30%) was further added to promote the

conversion of Sn^{2+} to Sn^{4+} before the hydrothermal treatment at 160 °C, while for SnO, the solution was purged with N_2 before the treatment.

2.2 Characterization

X-ray diffraction patterns of the samples were recorded on a Brucker D8 Advance diffractometer. UV-visible diffuse reflection spectra (UV-vis DRS) were recorded on a Vis-NIR spectrophotometer (TU-1950, Persee) with $BaSO_4$ as a reference. Simultaneous thermal gravimetric analysis (TGA) and differential thermal analysis (DTA) of the Sn^{2+}–SnO_2 prepared at different temperatures were performed on a Shimadzu DTG-60H TG/DTA thermal analyser. N_2 adsorption–desorption isotherms were obtained at 77 K by using a Micromeritics ASAP 2020 surface area analyzer. The morphologies were examined by a scanning electron microscopy (SEM, JSM-6610LV, Hitachi) and a transmission electron microscopy (TEM, FEI Tecnai G2 F20 S-TWIN). X-ray photoelectron spectroscopy (XPS) analysis was conducted on an ESCALAB 250 photoelectron spectrometer (Thermo Fisher Scientific) using Al Kα X-ray beam (1486.6 eV).

2.3 Photocatalytic decolorization of MO

Photocatalytic degradation of MO solution was carried out in a tubular reactor which was surrounded by a water cooling jacket. A 300 W Xe lamp (CEL-HXF300) was used as a light source with a UV cut off filter ($\lambda > 400$ nm). The picture of the reaction system can be found in Fig. S1 (see ESI†). In a typical experiment, 100 mg sample was dispersed in 100 mL 10 ppm MO. The suspension was then stirred for 30 min in the dark to reach an adsorption–desorption equilibrium. During irradiation, the solution temperature was controlled at 20 °C by a Julabo F12 cooling bath (Julabo Labortechnik, Germany). 3.8 mL suspension was withdrawn through a pipette every 10 min. The residual MO in the supernatant was monitored by a spectrophotometer (TU-1950, Persee).

2.4 Measurements of the photocurrent and the formation of hydroxyl radicals (˙OH)

The photocurrent test was conducted on a CHI 660E electrochemical workstation (Chenhua, Shanghai) in a conventional three-electrode cell with Pt wire as the counter electrode, Ag/AgCl electrode as the reference electrode, and the samples as the working electrode. The working electrode was fabricated by drop casting the sample powder dispersed water onto a FTO glass substrate (0.6 × 0.6 cm) followed by drying the electrode at room temperature. 0.2 M Na_2SO_4 aqueous solution was used as the electrolyte.

The formations of ˙OH in the photocatalytic process were determined by photoluminescence (PL) technique with terephthalic acid (TA) as a probe molecule. The procedure was similar to the degradation of MO except that the solution was replaced by 100 mL 5×10^{-4} M TA and 2×10^{-3} M NaOH mixed solution. The fluorescence signal of TAOH adduct was measured by a fluorescence spectrophotometer (JASCO FP-6500).

3. Results and discussion

3.1 Characterization of Sn^{2+}–SnO_2 and SnO_2

Fig. 1a shows the XRD patterns of Sn^{2+}–SnO_2 prepared at different hydrothermal temperature. The diffraction peaks can be assigned to tetragonal SnO_2 (JCPDS No. 77-447). The broad peaks at 2θ ca. 27, 34, and 52° can be ascribed to the reflections of the (110), (101), and (211) planes of SnO_2.[46] The intensity of these peaks improves gradually with the hydrothermal temperature, indicating that the crystallization of SnO_2 is favoured by an elevated temperature. The top of Fig. 1a shows the XRD pattern of the prepared SnO_2. The diffraction peak can be assigned to tetragonal SnO_2 and are more pronounced and sharpened than the sample prepared in pure H_2O. This result suggests that, besides the conversion of Sn^{2+} to Sn^{4+}, the crystallization of SnO_2 was also promoted by the addition of H_2O_2. Similar function of H_2O_2 has been reported.[47,48]

Fig. 1b shows the UV-vis DRS spectra of the Sn^{2+}–SnO_2. An absorption threshold at ca. 500 nm can be observed and the absorption edge shows a blue-shift with the hydrothermal temperature. A change of the samples color from pale yellow to slight brown then can be observed (see the inset of Fig. 1b).
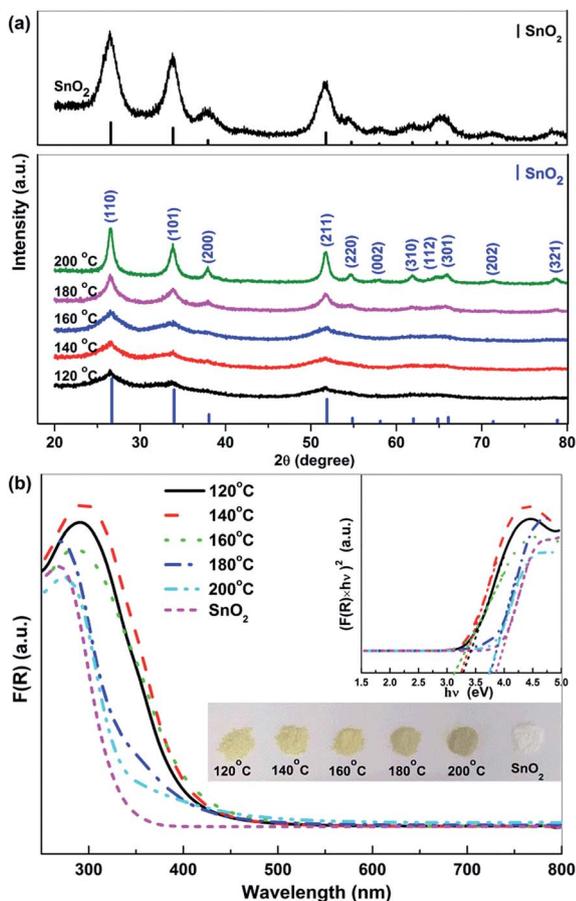
Fig. 1 (a) X-ray diffraction patterns and (b) UV-vis DRS spectra of the Sn^{2+}–SnO_2 prepared at different temperatures and SnO_2. The inset of (b) shows the corresponding Tauc plots and the appearance of the samples.

Although the samples show the same tetragonal structure as that of pristine SnO_2, their colour is quite darker than SnO_2, indicating the doping of Sn^{2+}.[11] As shown in the inset of Fig. 1b, Tauc plot approach[49] was used to determine Sn^{2+}–SnO_2 band gap energy (E_g). The results (summarized in Table 1) indicate that, for the samples prepared below 160 °C, the E_g is only ca. 3.10 eV. Further enhancing the hydrothermal temperature to 200 °C, the samples E_g are close to 3.60 eV. The E_g of the prepared SnO_2 is 3.73 eV and it is consistent well with the reported value.[41,50–53] This result clearly indicates that the absorption of SnO_2 could be extended to the visible light region by doping with Sn^{2+}.[11,41] As Sn^{2+} tends to be oxidized to Sn^{4+} at an elevated temperature, the increase of E_g with hydrothermal temperature should be caused by the reduction of Sn^{2+} doping content.

$SnO_2 \cdot H_2O$ shows a similar diffraction pattern to the tetragonal SnO_2.[50] TGA and DTA analyses of the prepared Sn^{2+}–SnO_2 were carried out to further corroborate the identification. As shown in Fig. 2a, an initial mass loss of 1.0% can be observed below 120 °C. It can be attributed to the dehydration of the adsorbed water, which leads to the endothermic peak in Fig. 2b. A second mass loss ca. 1.0% is occurred around 400 °C due to the volatilization of the contaminated Cl^-. After that, the TGA curves have no change. The result rules out the possibility that the products are $SnO_2 \cdot H_2O$ as its theoretical weight loss is larger than 10%. It also rules out the presence of SnO component in the samples, which shows a weight increases around 570 °C[54] due to the oxidation of Sn^{2+} to Sn^{4+}. Thus, based on the results shown in Fig. 1 and 2, it can be deduced that the samples prepared at different temperatures in H_2O are Sn^{2+}–SnO_2.

Fig. 3 shows the SEM images of the prepared Sn^{2+}–SnO_2. The samples prepared below 200 °C (Fig. 3a–d) are mainly composed of rods with a length of about 15 μm and a diameter of about 3 μm. With enhancing the preparation temperature, the surface of the rods becomes coarse and some small particles are present, suggesting the decomposition of the rods. When the temperature reaches 200 °C, no any rods can be observed (Fig. 3e). Pristine SnO_2 prepared in the H_2O_2-contained solution (Fig. 3f) shows a similar morphology feature as the sample prepared at 200 °C.
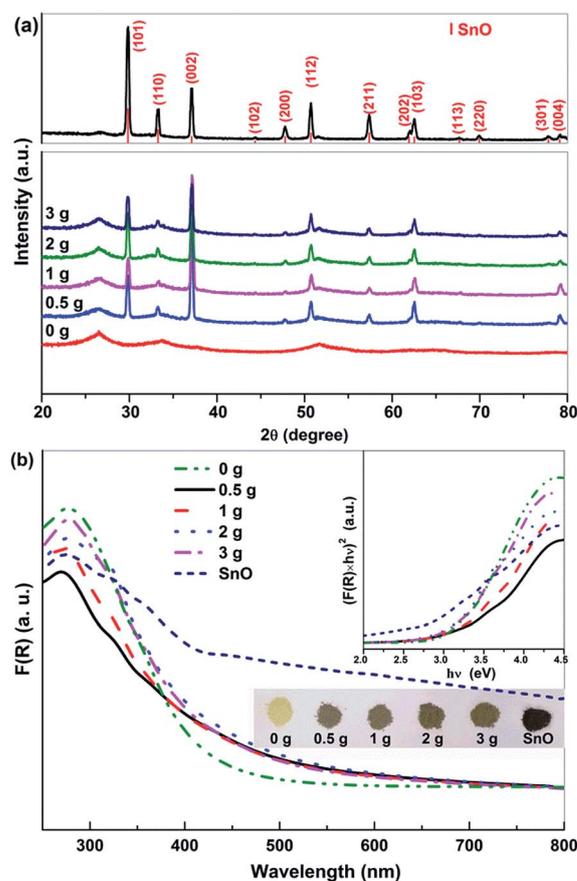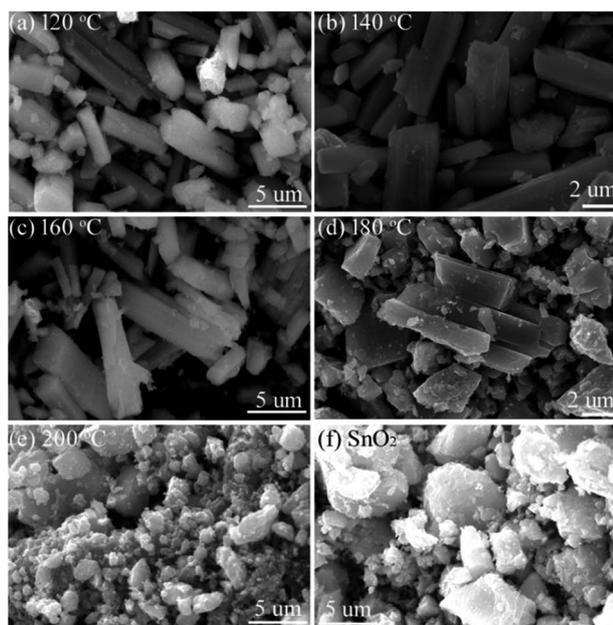
3.2 Characterization of SnO/SnO_2 and SnO

Fig. 4a shows the XRD patterns of the SnO/SnO_2 prepared in different urea-contained solutions. When no urea was added, the resulted sample was Sn^{2+}–SnO_2 as shown by Fig. 1. For the samples prepared in urea-contained solution, two sets of diffraction peaks originated from tetragonal SnO_2 (JCPDS No. 77-447) and SnO (JCPDS No. 78-1913) can be observed, confirming the formation of SnO/SnO_2 composite. As shown in the top of Fig. 4a, the diffraction pattern of the sample prepared in N_2 purged solution can be assigned to SnO, along with two very small diffraction peaks of SnO_2 (110) and (211).

Fig. 4b shows the UV-vis DRS of the prepared SnO–SnO_2 and SnO. The composite show an apparent visible light absorption and the thresholds extend to ca. 700 nm. With an increase of urea dosage, the absorption coefficient of the resulted SnO–

Table 1 Summary of the hydrothermal conditions and the characterization results of the E_g and the BET surface area of the prepared Sn oxides

Reaction condition		Product	E_g (eV)	BET area (m^2 g^{-1})
Temp. (°C) (without urea)	120	Sn^{2+}–SnO$_2$	3.20	100.1
	140		3.13	—
	160		3.10	116.4
	180		3.59	—
	200		3.60	99.9
Urea (g) (temp. 160 °C)	0	Sn^{2+}–SnO$_2$	3.14	116.4
	0.5	SnO/SnO$_2$	3.41	—
	1.0		3.34	79.2
	2.0		3.04	—
	3.0		3.08	77.1
3 g urea + 1 mL H$_2$O$_2$, 160 °C		SnO$_2$	3.73	173.3
3 g urea + N$_2$ purged, 160 °C		SnO	2.71	5.2
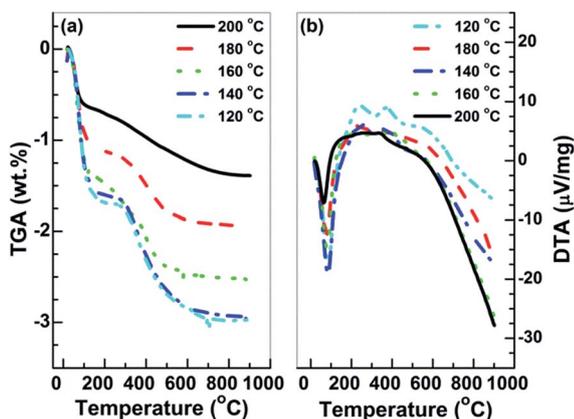
Fig. 2 (a) TGA and (b) DTA curves of the SnO$_2$ prepared at different temperatures.

Fig. 3 SEM images of the samples prepared at different temperatures (a) 120, (b) 140, (c) 160, (d) 180, (e) 200 °C, and (f) SnO$_2$ prepared at 160 °C in H$_2$O$_2$-contained solution.

Fig. 4 (a) X-ray diffraction patterns and (b) UV-vis DRS spectra of the SnO/SnO$_2$ composites prepared in different urea-containing solutions and the prepared SnO. The inset shows the corresponding Tauc plots and the appearance of the samples.

SnO$_2$ is improved and the sample colour changes from slight brown to dark brown as shown in the inset of Fig. 4b. The absorption of SnO/SnO$_2$ is gradually extended to the visible range with an increase of urea dosage. SnO shows the highest visible light absorption coefficient due to its black colour and the E_g is 2.71 eV, agreeing well with the reported result.[1] The E_g

of SnO/SnO$_2$ samples were estimated by Tauc plots (the inset of Fig. 4b) and the results are summarized in Table 1.

Fig. 5 shows the SEM images of the prepared SnO/SnO$_2$. Resembling the sample prepared in water (without urea, Fig. 5a), rod-like samples (Fig. 5b–e) with a length of about 15 μm and a diameter of about 3 μm were also obtained in the urea-contained solution. However, a decomposition of the rods can be observed with an increase of urea dosage and the surface becomes rough (Fig. 5b–e). Some small particles then appear and distribute on the rods surface. As shown in Fig. 5f, the morphology of the prepared SnO is quite different to SnO/SnO$_2$ composites. The sample is composed of many tightly aggregated strips.

The morphology feature of the SnO/SnO$_2$ was further characterized by TEM using the sample prepared in 3 g urea-contained solution as a representative. As shown in Fig. 6a and b, some nanosheets and small rods with a diameter of *ca.* 10 nm and a length of *ca.* 300 nm (indicated by the arrows in Fig. 6b) can be observed. The small rods are covered by the nanosheets. The SAED pattern in Fig. 6c indicates the polycrystalline nature of the nanosheets. The diffraction rings from the inner to outward can be indexed to the (110), (101), (200), and (211) planes of SnO$_2$, respectively. Two sets of lattice space with *d* values of 0.26 and 0.33 nm can be found in the HRTEM images (Fig. 6d and e), which corresponds to the (101) and (110) planes of tetragonal SnO$_2$. The results suggest that the sheet-like particles are SnO$_2$. As for the small rods, the HRTEM image (Fig. 6f) demonstrates that the *d* value of the lattice space is 0.29 nm, which corresponds to the (101) plane of SnO.[43] Thus, the small rods are SnO. Similar structure of SnO has been reported in SnO/SnO$_2$ composite.[40]
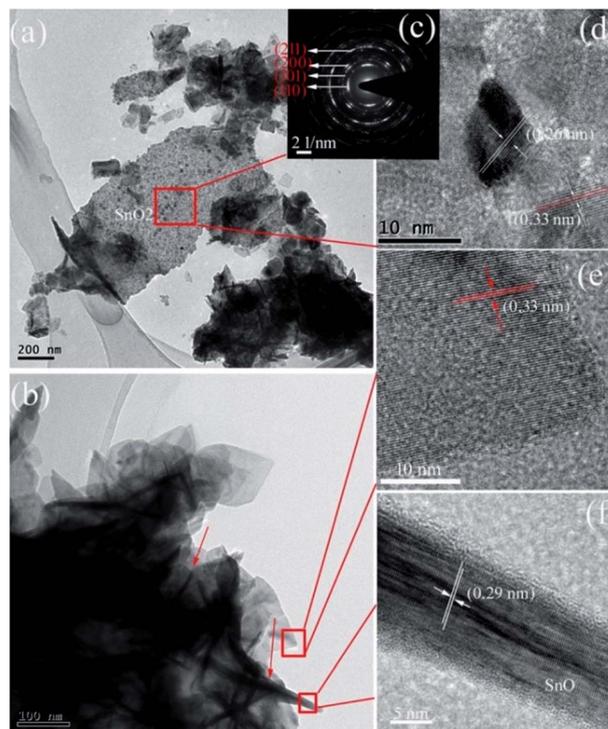
Fig. 6 (a and b) TEM, (c) SAED, and (d–f) HRTEM images of the prepared SnO–SnO$_2$ in 3 g urea-contained solution.

Some of the prepared samples including SnO$_2$, Sn^{2+}–SnO$_2$, SnO/SnO$_2$ and SnO were analyzed by XPS to study the chemical states of Sn and O. The survey spectra (Fig. S2-a†) clearly indicate that, besides the adventitious C, the samples are composed of Sn and O. The double peaks located at the binding energy of 486.7 and 495.2 eV with a spin–orbit splitting energy of 8.5 eV can be ascribed to the Sn 3d$_{5/2}$ and Sn 3d$_{3/2}$, respectively. As shown in Fig. 7, except for SnO$_2$, the Sn 3d$_{5/2}$ peak can be
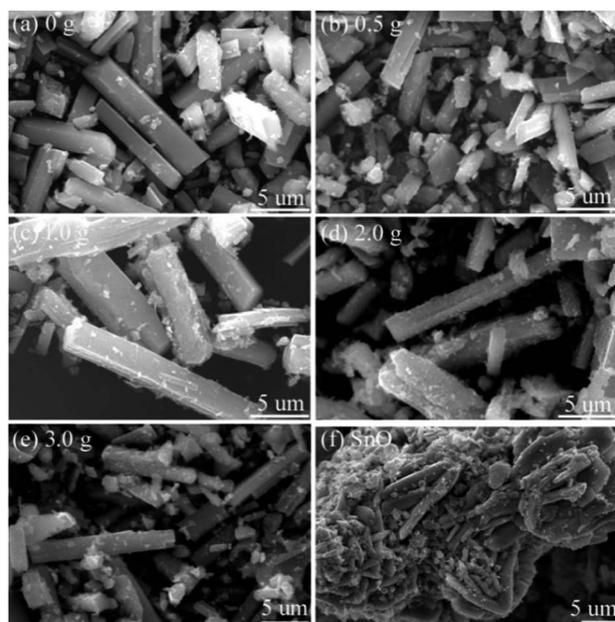
Fig. 5 SEM images of the samples prepared in different urea-contained solutions (a) 0, (b) 0.5, (c) 1.0, (d) 2.0, (e) 3.0 g, and (f) the prepared SnO.
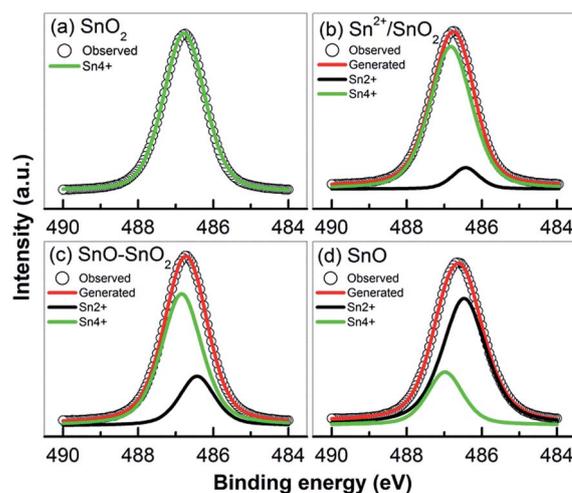
Fig. 7 High resolution XPS of Sn 3d$_{5/2}$ peak taken form (a) SnO$_2$, (b) Sn^{2+}–SnO$_2$ (prepared at 160 °C), (c) SnO/SnO$_2$ (prepared in 3 g urea added solution), and (d) SnO.
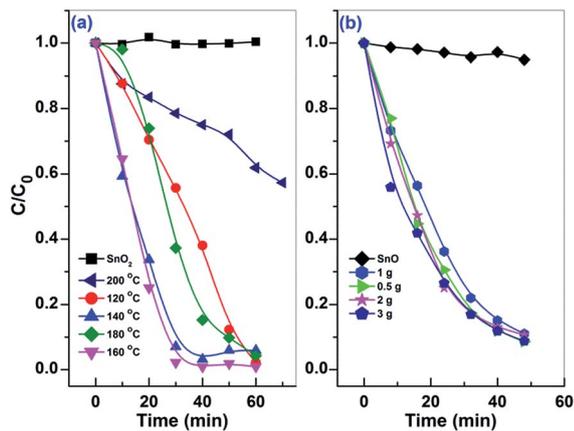
Fig. 8 The temporal changes of MO concentration with irradiation time over the (a) Sn^{2+}–SnO_2 prepared at different temperatures and SnO_2, and (b) SnO/SnO_2 prepared in different urea-contained solutions and SnO.

The photocatalytic stability of Sn^{2+}–SnO_2 and SnO/SnO_2 was investigated by reusing the photocatalysts. Unfortunately, as shown in Fig. 9, a deactivation of the samples can be observed. The activity can sustain for 3 runs on Sn^{2+}–SnO_2, while on SnO/ SnO_2, it can only sustain for 1 run. Considering that the visible light photocatalytic activity is originated from Sn^{2+} species and the oxidation potential of Sn^{2+} to Sn^{4+} is only 0.15 V (*vs.* SHE),[11,41] the deactivation of the samples is caused by the oxidation of Sn^{2+} to Sn^{4+} during the reaction.

3.4 Proposed reaction mechanism

The photocurrents of the prepared Sn^{2+}–SnO_2, SnO/SnO_2, SnO, and SnO_2 were measured under visible light irradiation to

investigate the generation and the separation of the photo-induced charge carriers. As shown in Fig. 10, only Sn^{2+}–SnO_2 and SnO/SnO_2 show apparent reversible photocurrent responses with light on and off. The result confirms that a visible light response can be involved by doping SnO_2 with Sn^{2+} or coupling it with SnO. Surprisingly, although SnO/SnO_2 shows a comparable photocatalytic activity to Sn^{2+}–SnO_2, the photocurrent density of SnO/SnO_2 is substantially lower than the latter. A decay of the photocurrent with irradiation time can be observed on both of the samples, further suggesting their instability. Although SnO shows a visible light absorption, the photocurrent is negligible. It seems that the photo-induced charge carriers are consumed by SnO itself, rather than migrating to the surface to form a current. This may be the reason why SnO shows quite low performance for the decolorization of MO (Fig. 8b) and the activity of SnO/SnO_2 can only sustain for one run (Fig. 9b). The photocurrent of SnO_2 is negligible as it cannot be activated under visible light.

The photocurrent results suggest that the charge carriers can be generated on Sn^{2+}–SnO_2 and SnO/SnO_2 under visible light irradiation. These charge carriers can further react with the adsorbed –OH, H_2O, and O_2 to form the active radicals. $^\bullet OH$ is one of the key active species for the degradation of pollutants. According to the band structures of SnO/SnO_2 and Sn^{2+}–SnO_2 (Fig. S6†), $^\bullet OH$ can be induced by the photogenerated h^+ in these samples as the standard reduction potential of $^\bullet OH/–OH$ is 1.99 V. $^\bullet OH$ formed on these samples was trapped by TA. As shown in Fig. S7,† the characterized fluorescence peak of TAOH at 425 nm can be observed on the prepared Sn^{2+}–SnO_2 (Fig. S7a–e†) and SnO/SnO_2 (Fig. S7g–k†) and the signal increases gradually with irradiation time. It suggests that the prepared Sn^{2+} incorporated SnO_2 samples have the capability to form $^\bullet OH$ under the visible light irradiation. For SnO, the formation of TAOH is far slower than the Sn^{2+} incorporated SnO_2 samples and ceased after irradiation for *ca.* 25 min. Other control tests indicated that the formation of $^\bullet OH$ on SnO_2 is negligible and cannot be perceived for the tests without a photocatalyst or illumination (Fig. S7m–o†). The formation efficiency of $^\bullet OH$ on
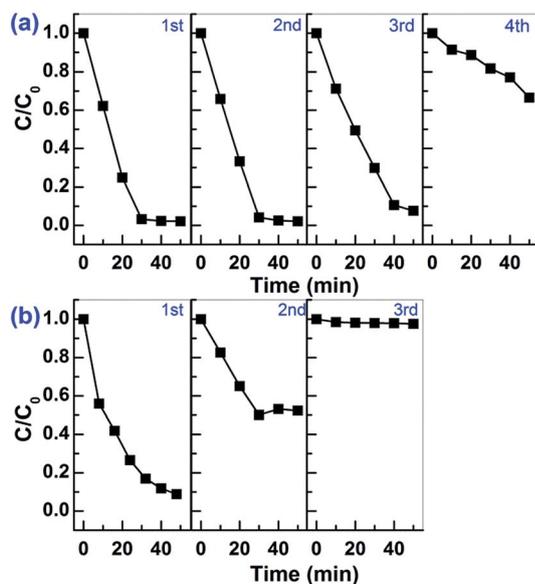

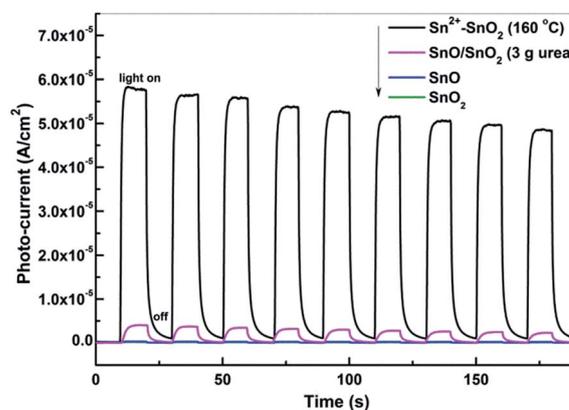Fig. 9 Cycling tests for the photocatalytic decolorization of MO on (a) Sn^{2+}–SnO_2 prepared at 160 °C and (b) SnO–SnO_2 prepared in 3 g urea added solution.

Fig. 10 Photocurrent responses of Sn^{2+}–SnO_2 prepared at 160 °C, SnO/SnO_2 prepared in 3 g urea added solution, SnO, and SnO_2 under visible light irradiation ($\lambda > 400$ nm).

the prepared Sn^{2+}–SnO_2 and SnO/SnO_2 samples is generally in agreement with their photocatalytic performances shown in Fig. 8. This relevance suggests that at least ˙OH accounts for the degradation of MO. The visible-light-induced e^- and h^+ are aroused by the doping of Sn^{2+} (ref. 41) or the coupling of SnO component[38,40,61] (the electronic contributions from 5s orbitals of Sn^{2+}). These charge carriers can be trapped by O_2, H_2O, or adsorbed –OH to generate ˙OH or other oxidative species, which eventually lead to the decomposition of MO. Besides, Sn^{2+} also can be oxidized to Sn^{4+} by these oxidative species, leading to the deactivation of Sn^{2+}–SnO_2 and SnO/SnO_2 (Fig. 9).

4. Conclusions

We have developed a simple and effective hydrothermal method to selective preparation of SnO_2, Sn^{2+}–SnO_2, SnO/SnO_2, and SnO with $SnCl_2$ as precursor. Through adding H_2O_2 or urea, the solution can be tuned from an O_2-rich to O_2 deficient atmosphere, which facilitates the transformation of Sn^{2+} to SnO_2 and the preservation of Sn^{2+} (in a form of doping Sn^{2+} or SnO component), respectively. The absorption of SnO_2 can be successfully extended to the visible light region after self-doping with Sn^{2+} or coupling with SnO, which endows a visible light photocatalytic activity for MO degradation. Unfortunately, due to the oxidation of Sn^{2+} to Sn^{4+}, the activities of the samples are quite unstable. Further work is still required to improve their photo-stability. Nonetheless, we believe that this work provides a simple method to selective preparation of different Sn-based oxides, which is essential for their applications, such as the detection of NO and NO_2 based on SnO or SnO_2.[61] The work also provides a useful concept that is, through controlling the atmosphere of the solution, the oxidation state of metal oxides can be readily tuned by a hydrothermal method.

Acknowledgements

Notes and references

1 W. Xia, H. Wang, X. Zeng, J. Han, J. Zhu, M. Zhou and S. Wu, *CrystEngComm*, 2014, **16**, 6841–6847.

2 E. Comini, *Anal. Chim. Acta*, 2006, **568**, 28–40.

3 H. B. Wu, J. S. Chen, H. H. Hng and X. W. Lou, *Nanoscale*, 2012, **4**, 2526–2542.

4 K. Ellmer, *Nat. Photonics*, 2012, **6**, 809–817.

5 J. S. Chen and X. W. Lou, *Small*, 2013, **9**, 1877–1893.

6 M. Batzill and U. Diebold, *Prog. Surf. Sci.*, 2005, **79**, 47–154.

7 Y. Idota, T. Kubota, A. Matsufuji, Y. Maekawa and T. Miyasaka, *Science*, 1997, **276**, 1395–1397.

8 H. Wang and A. L. Rogach, *Chem. Mater.*, 2014, **26**, 123–133.

9 Z. Han, N. Guo, F. Li, W. Zhang, H. Zhao and Y. Qian, *Mater. Lett.*, 2001, **48**, 99–103.

10 S. Mathur, R. Ganesan, I. Grobelsek, H. Shen, T. Ruegamer and S. Barth, *Adv. Eng. Mater.*, 2007, **9**, 658–663.

11 H. Wang, K. Dou, W. Y. Teoh, Y. Zhan, T. F. Hung, F. Zhang, J. Xu, R. Zhang and A. L. Rogach, *Adv. Funct. Mater.*, 2013, 4847–4853, DOI: 10.1002/adfm.201300303.

12 Z. Li, Y. Zhou, T. Yu, J. Liu and Z. Zou, *CrystEngComm*, 2012, **14**, 6462–6468.

13 A. Kar, S. Sain, S. Kundu, A. Bhattacharyya, S. Kumar Pradhan and A. Patra, *ChemPhysChem*, 2015, **16**, 1017–1025.

14 A. K. Sinha, M. Pradhan, S. Sarkar and T. Pal, *Environ. Sci. Technol.*, 2013, **47**, 2339–2345.

15 Z. D. Li, Y. Zhou, J. C. Song, T. Yu, J. G. Liu and Z. G. Zou, *J. Mater. Chem. A*, 2013, **1**, 524–531.

16 D. Chu, J. Mo, Q. Peng, Y. Zhang, Y. Wei, Z. Zhuang and Y. Li, *Chemcatchem*, 2011, **3**, 371–377.

17 M. Wang, Y. Gao, L. Dai, C. Cao and X. Guo, *J. Solid State Chem.*, 2012, **189**, 49–56.

18 S. Wu, H. Cao, S. Yin, X. Liu and X. Zhang, *J. Phys. Chem. C*, 2009, **113**, 17893–17898.

19 H. Chen, C. E. Nanayakkara and V. H. Grassian, *Chem. Rev.*, 2012, **112**, 5919–5948.

20 M. R. Hoffmann, S. T. Martin, W. Y. Choi and D. W. Bahnemann, *Chem. Rev.*, 1995, **95**, 69–96.

21 Y. C. Zhang, L. Yao, G. S. Zhang, D. D. Dionysiou, J. Li and X. H. Du, *Appl. Catal., B*, 2014, **144**, 730–738.

22 Y. C. Zhang, Z. N. Du, K. W. Li, M. Zhang and D. D. Dionysiou, *ACS Appl. Mater. Interfaces*, 2011, **3**, 1528–1537.

23 Y. Zhao, Y. Zhang, J. Li and Y. Chen, *Sep. Purif. Technol.*, 2014, **129**, 90–95.

24 K. Vinodgopal and P. V. Kamat, *Environ. Sci. Technol.*, 1995, **29**, 841–845.

25 N. Chadwick, S. Sathasivam, A. Kafizas, S. M. Bawaked, A. Y. Obaid, S. Al-Thabaiti, S. N. Basahel, I. P. Parkin and C. J. Carmalt, *J. Mater. Chem. A*, 2014, **2**, 5108–5116.

26 L. Zheng, Y. Zheng, C. Chen, Y. Zhan, X. Lin, Q. Zheng, K. Wei and J. Zhu, *Inorg. Chem.*, 2009, **48**, 1819–1825.

27 W. Cun, X. M. Wang, B. Q. Xu, J. C. Zhao, B. X. Mai, P. Peng, G. Y. Sheng and H. M. Fu, *J. Photochem. Photobiol., A*, 2004, **168**, 47–52.

28 J. Wang, H. Li, S. Meng, L. Zhang, X. Fu and S. Chen, *Appl. Catal., B*, 2017, **200**, 19–30.

29 H. Ullah, A. Khatoon and Z. Akhtar, *Mater. Res. Express*, 2014, **1**, 045001.

30 D. Qi, L. Lu, Z. Xi, L. Wang and J. Zhang, *Appl. Catal., B*, 2014, **160–161**, 621–628.

31 I. S. Chae, M. Koyano, K. Oyaizu and H. Nishide, *J. Mater. Chem. A*, 2013, **1**, 1326–1333.

32 A. Wahl and J. Augustynski, *J. Phys. Chem. B*, 1998, **102**, 7820–7828.

33 J. Jiang, L. Z. Zhang, H. Li, W. W. He and J. J. Yin, *Nanoscale*, 2013, **5**, 10573–10581.

34 Y. Hosogi, Y. Shimodaira, H. Kato, H. Kobayashi and A. Kudo, *Chem. Mater.*, 2008, **20**, 1299–1307.

35 A. Naldoni, M. Allieta, S. Santangelo, M. Marelli, F. Fabbri, S. Cappelli, C. L. Bianchi, R. Psaro and V. Dal Santo, *J. Am. Chem. Soc.*, 2012, **134**, 7600–7603.

36 T. Xia and X. B. Chen, *J. Mater. Chem. A*, 2013, **1**, 2983–2989.

37 A. Iwaszuk and M. Nolan, *J. Mater. Chem. A*, 2013, **1**, 6670–6677.

38 A. K. Sinha, P. K. Manna, M. Pradhan, C. Mondal, S. M. Yusuf and T. Pal, *RSC Adv.*, 2014, **4**, 208–211.

39 K. Santhi, C. Rani and S. Karuppuchamy, *J. Alloys Compd.*, 2016, **662**, 102–107.

40 A. Roy, S. Arbuj, Y. Waghadkar, M. Shinde, G. Umarji, S. Rane, K. Patil, S. Gosavi and R. Chauhan, *J. Solid State Electrochem.*, 2016, 1–9, DOI: 10.1007/s10008-016-3328-y.

41 C. M. Fan, Y. Peng, Q. Zhu, L. Lin, R. X. Wang and A. W. Xu, *J. Phys. Chem. C*, 2013, **117**, 24157–24166.

42 Y. He, D. Li, J. Chen, Y. Shao, J. Xian, X. Zheng and P. Wang, *RSC Adv.*, 2014, **4**, 1266–1269.

43 Q. Yan, J. Wang, X. Han and Z. Liu, *J. Mater. Res.*, 2013, **28**, 1862–1869.

44 G. Chen, S. Ji, Y. Sang, S. Chang, Y. Wang, P. Hao, J. Claverie, H. Liu and G. Yu, *Nanoscale*, 2015, **7**, 3117–3125.

45 H. Uchiyama, H. Ohgi and H. Imai, *Cryst. Growth Des.*, 2006, **6**, 2186–2190.

46 J. R. Sambrano, L. A. Vasconcellos, J. B. L. Martins, M. R. C. Santos, E. Longo and A. Beltran, *J. Mol. Struct.: THEOCHEM*, 2003, **629**, 307–314.

47 J. Mazloom, F. E. Ghodsi and H. Golmojdeh, *J. Alloys Compd.*, 2015, **639**, 393–399.

48 X. Fu, D. Y. C. Leung and S. Chen, *CrystEngComm*, 2014, **16**, 616–626.

49 J. Tauc, R. Grigorovici and A. Vancu, *Phys. Status Solidi*, 1966, **15**, 627–637.

50 T. Arai and S. Adachi, *ECS J. Solid State Sci. Technol.*, 2012, **1**, R15–R21.

51 Z. Khodami and A. Nezamzadeh-Ejhieh, *J. Mol. Catal. A: Chem.*, 2015, **409**, 59–68.

52 H. Chen, L. Ding, W. Sun, Q. Jiang, J. Hu and J. Li, *RSC Adv.*, 2015, **5**, 56401–56409.

53 L. Zhang, H. Zhang, H. Huang, Y. Liu and Z. Kang, *New J. Chem.*, 2012, **36**, 1541–1544.

54 G. Sun, N. Wu, Y. Li, J. Cao, F. Qi, H. Bala and Z. Zhang, *Mater. Lett.*, 2013, **98**, 234–237.

55 G. Zhou, X. Wu, L. Liu, X. Zhu, X. Zhu, Y. Hao and P. K. Chu, *Appl. Surf. Sci.*, 2015, **349**, 798–804.

56 V. B. R. Boppana and R. F. Lobo, *J. Catal.*, 2011, **281**, 156–168.

57 H.-R. Kim, K.-I. Choi, J.-H. Lee and S. A. Akbar, *Sens. Actuators, B*, 2009, **136**, 138–143.

58 W. K. Choi, H. Sung, K. H. Kim, J. S. Cho, S. C. Choi, H. J. Jung, S. K. Koh, C. M. Lee and K. Jeong, *J. Mater. Sci. Lett.*, 1997, **16**, 1551–1554.

59 T. Tasaki, T. Wada, K. Fujimoto, S. Kai, K. Ohe, T. Oshima, Y. Baba and M. Kukizaki, *J. Hazard. Mater.*, 2009, **162**, 1103–1110.

60 T. X. Wu, G. M. Liu, J. C. Zhao, H. Hidaka and N. Serpone, *J. Phys. Chem. B*, 1998, **102**, 5845–5851.

61 L. Li, C. Zhang and W. Chen, *Nanoscale*, 2015, 7, 12133–12142.